IEEE Access
Multidisciplinary ⋮ Rapid Review ⋮ Open Access Journal

Received March 29, 2022, accepted April 20, 2022, date of publication April 22, 2022, date of current version April 28, 2022.

Digital Object Identifier 10.1109/ACCESS.2022.3169888

Design and Control of a Transverse Flux Linear Switched Reluctance Machine for Rail Transit Application

XINLIANG LI[1], FANG LIU[2], WEI JIANG[1], (Member, IEEE), HONG JIN[1], MINYAN LI[1], AND QIANLONG WANG[1]

[1]College of Electrical, Energy and Power Engineering, Yangzhou University, Yangzhou 225000, China
[2]College of Information Engineering, Yangzhou Polytechnic Institute, Yangzhou 225000, China

Corresponding author: Qianlong Wang (wangqianlong@yzu.edu.cn)

This work was supported in part by the Yangzhou City-Yangzhou University Joint Fund under Grant YZ2020169.

ABSTRACT The design, optimization and control methods of a transverse flux Linear Switched Reluctance Motor (LSRM) for the rail transit application are introduced. Two structures of LSRMs, EI type and EE type, are compared and analyzed. The structure of EE type machine is optimized from the perspective of average electromagnetic thrust per unit mass through finite element calculations. The initial sizes of the motor are calculated according to the design theory of the rotary SRM. After obtaining the initial sizes, the sensitivities of the LSRM sizes are analyzed by the three-dimensional finite element calculation, and then the sizes such as the slot depth, the slot width and the tooth width of the motor are optimized. The hardware test platform is built, the electromagnetic characteristics of the prototype are tested, and the motor characteristics of the LSRM with different secondary materials are compared. The control method of the LSRM with position sensors is proposed, and then the sensorless control of the motor is also realized based on the pulse injection strategy. The experimental results verify the effectiveness of the design and control strategies.

INDEX TERMS Switched reluctance, transverse flux, linear motor, sensorless control.

I. INTRODUCTION

The wheel rail train driven by the linear motor is an important developing direction of the urban traffic in the future. At present, the linear induction motor and the linear synchronous motor are mainly used in the rail transit. Among them, the linear induction motor has the problems of edge effects and low power factor [1], and the cost of synchronous motor is relatively high [2]. The high cost of permanent magnet materials limits the application of permanent magnet linear motors in the field of long stroke rail transit [3]. Linear Switched Reluctance Motor (LSRM), as shown in Figure 1, can adopt transverse flux and block secondary structure, the secondary of which doesn't have to be processed into cogging structure. The cogging effect can be naturally formed by using intermittent solid steel plates as the secondary. Therefore, the LSRM has the merits of low cost and high reliability, and it has been one of the optional motors for rail transit traction system [4], [5].

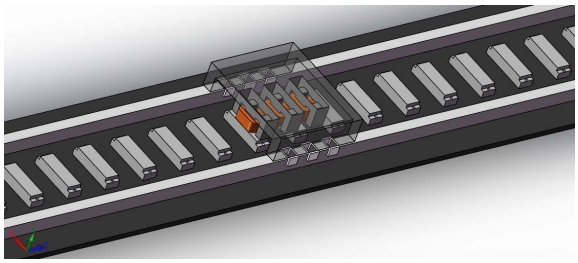

FIGURE 1. Structural diagram of LSRM prototype for rail transit.

The main advantages of LSRMs are simple and rugged structure and low manufacturing cost. The motors contain no permanent magnet and only concentrated winding on the primary cores, which makes them suitable for strong vibration and high temperature conditions. The excitation currents are unipolar, the power converter has no danger of direct

The associate editor coordinating the review of this manuscript and approving it for publication was Ton Duc Do.

short circuit, and there is no need for the dead-time control. Many scholars have conducted detailed research on the size calculation [6], optimization [7], [8], modeling [9], characteristic analysis [10], [11], and control strategy [12], [13] of LSRMs/SRMs. The main applications of the motor include wave power generation [14], [15], vertical elevator [16], [17], electromagnetic ejection [18] and rail transit [19]–[21]. In [19], a segmental-type LSRM with a toroidally wound mover was proposed for the first time, which can be applied to the field of rail transit. Novel LSRM structures which can be applied to rail transit are also proposed in [20] and [21].

The study on the LSRMs is still in the laboratory research stage. The structural design of the LSRMs mainly refers to the design methods of the rotary SRMs, and the parameters of LSRMs are obtained through the size conversion of corresponding SRMs. The secondary of the LSRM laboratory prototype mostly adopts silicon steel sheet structure. The secondary made of silicon steel sheet lamination has high manufacturing cost, and the laying cost increases with the track travel. If the solid steels with high permeability are used as the secondary of the LSRM, the electromagnetic thrust is almost the same as that of the LSRM with silicon steel sheet structure, and the laying cost can be greatly reduced.

SRM/LSRM control systems usually need position sensors to provide real-time relative position information of the motor. The position sensors mainly include encoder, Hall element, photoelectric sensor and eddy current sensor. On the one hand, the position sensors increase the volume and manufacturing and maintenance cost of the system. On the other hand, the position sensors are vulnerable to external electromagnetic interference and will reduce the reliability of the drive system. The realization of sensorless control of the LSRM for rail transit will effectively improve the reliability of the system and reduce the maintenance cost of the rail transit system. The sensorless control strategies of the LSRMs usually refer to the control methods of SRMs. Therefore, similar to the SRMs, the LSRMs indirect position detection schemes can be divided into self-induction detection methods (e.g. pulse injection method, signal modulation method, current flux linkage method, current waveform monitoring method, current gradient method), mutual inductance detection methods, additional element methods (e.g. plate capacitance detection method, inverse series coil method) and artificial intelligence methods. The LSRM sensorless technologies in the medium and low speed field also mostly adopt the high-frequency pulse injection methods [22]–[24]. In [24], the sensorless control of a three-phase LSRM is realized by using the high-frequency pulse injection method, and its position estimation error is analyzed in detail. For the sensorless control system of bilateral silicon steel sheet structure LSRM, position identification methods based on coupling voltage [22] and eddy current effect [23] are proposed by our research group.

This paper attempts to apply a LSRM with high reliability, simple and solid structure and low cost to the traction field of medium and low-speed rail transit. Firstly, the optimal structures of the LSRMs in this application are compared and analyzed, and the calculation steps of the initial sizes of the prototype are given according to the selected motor structure. Based on the initial sizes, the three-dimensional finite element model is built by using the finite element software, the sensitivities of the initial sizes of the designed LSRM are analyzed, and the motor size parameters are optimized. Then the effects of different core materials on motor characteristics are compared and analyzed. Finally, the prototype is built, and the experiments of electromagnetic characteristic detection, position sensor control and position sensorless control are completed.

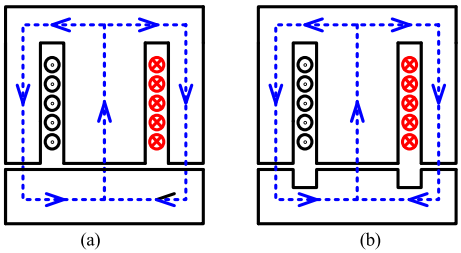

FIGURE 2. Winding setting and flux path distribution diagram of LSRM with (a) EI type, (b) EE type.

II. STRUCTURE SELECTION

The designed LSRM is applied to the field of long-distance rail transit. In order to reduce the laying cost of the secondary, the motor is preferably transverse magnetic flux, and the secondary is a block structure, as shown in Figure 1. The secondary of the linear motor with this structure doesn't need to be processed into cogging, intermittent block ferromagnetic materials can naturally form cogging effect, and the cost of processing, laying and maintenance is low.

The principle of the SRM/LSRM structure design is that the reluctance in the magnetic circuit should change as much as possible during the movement of the motor. According to the comparison results of transverse flux motor structures described in [25], the LSRM with E-type primary core has higher unit mass electromagnetic thrust than the LSRM with U-type primary structure. Therefore, two LSRM structures, EI type and EE type, are analyzed comparatively. Without considering the flux leakage, the coil winding direction and the flux closing path of two motors are shown in Figure 2. The comparisons between the two motors are carried out under the condition that the basic parameters such as motor voltage, current and coil turns are consistent.

When a constant excitation current of 10 A is applied to the primary coil of one phase, the flux density vector diagram of the primary and secondary of two LSRMs in the fully aligned position are shown in Figure 3 (a). The flux paths of the two LSRMs are the same, both of which are double circuits. A coil is wound around the middle teeth of the E-type primary. When the current is injected into the coil, the magnetic flux generated will go along the secondary teeth, secondary yoke and air gap to the left and right teeth of

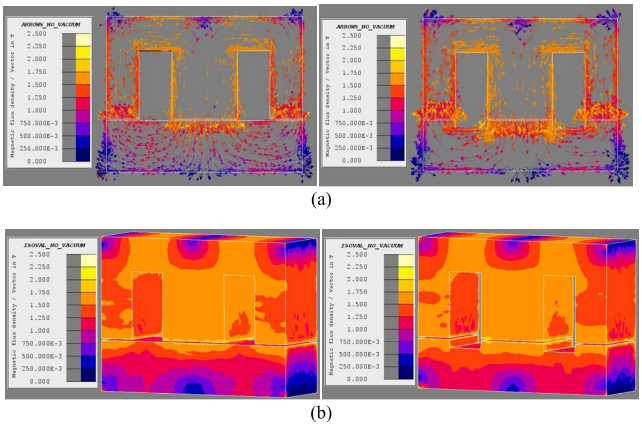

FIGURE 3. Comparison of EI type and EE type LSRMs (a) flux distribution, (b) flux density distribution.

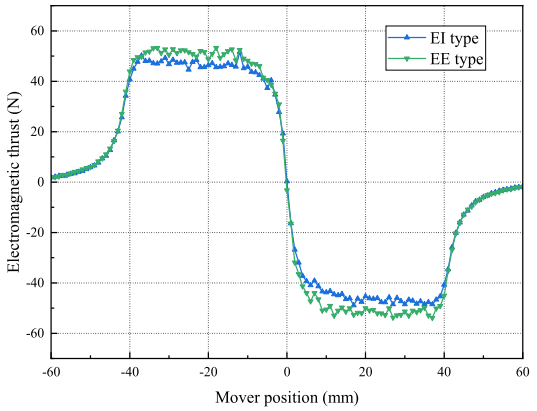

FIGURE 4. Electromagnetic thrust curves of two LSRMs.

TABLE 1. Comparison of electromagnetic thrusts of two LSRMs.

Type	V (dm^3)	m (kg)	$F/m\|_{avg}$ (N/kg)
EI	0.368	2.8074	8.5318
EE	0.36	2.808	9.2398

the E-type primary, and finally returns to the primary yoke to form a closed magnetic flux circuit. The primary and secondary magnetic densities of EI type and EE type are also similar, as shown in Figure 3 (b).

The static electromagnetic thrust comparison results of the two LSRMs are obtained through finite element simulation calculations. The results are shown in Figure 4. The peak value of electromagnetic thrusts of EE type LSRM is relatively larger. Considering the mass of the two LSRMs, the average electromagnetic thrusts per unit mass of the two motors are compared, and the results are shown in Table 1. It can be seen from the table that the average electromagnetic thrust per unit mass of EE type LSRM is increased by about 0.7 N/kg compared with the EI type LSRM. Therefore, EE type LSRM will be selected for further analysis in this paper.

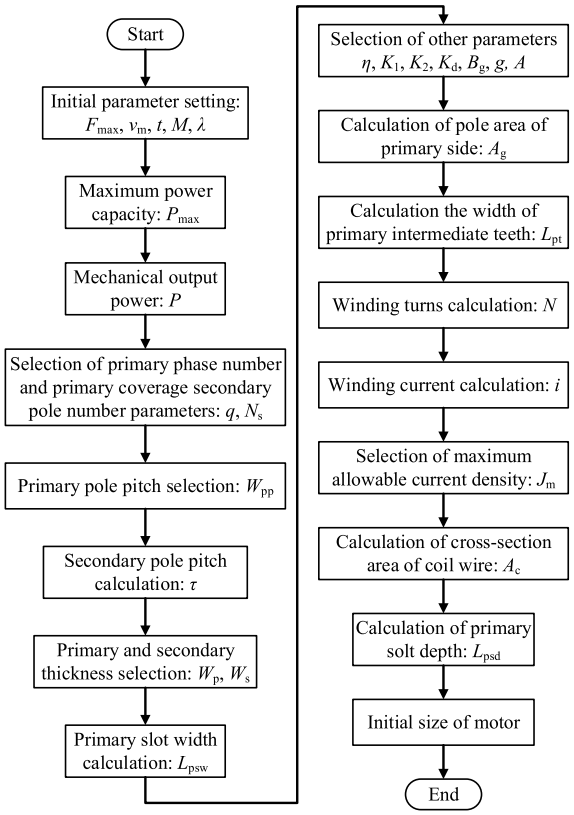

FIGURE 5. Flow chart of LSRM initial size calculation.

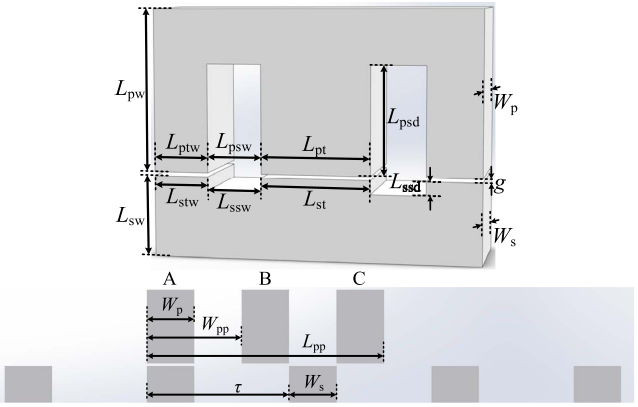

FIGURE 6. The dimensions of the designed LSRM.

III. INITIAL DIMENSIONS CALCULATION

Based on the motor selection results, the initial sizes of the selected LSRM are theoretically calculated, and the flow chart [5] of the calculation process is shown in Figure 5 below. The dimensions of the motor are shown in Figure 6.

The design objectives of the motor are: under rated operation, the maximum electromagnetic thrust of the motor $F_{max} = 64$ N, the maximum speed $v_m = 2.4$ m/s, the acceleration time $t = 1.5$ s, the maximum mass of the primary motor $M = 20$ kg, and the motor overload rate $\lambda = 2$.

The maximum power capacity of the designed machine $P_{max} = F_{max} \cdot v_m \approx 154$ W. The mechanical output power of the designed machine is

$$P = u \cdot i \cdot \eta \cdot K_d \tag{1}$$

where u and i are winding voltage and current, η is the efficiency, and the load factor K_d is deduced as

$$K_d = \frac{(x_{off} - x_{on}) \cdot q}{\tau} \tag{2}$$

where x_{on} is the conduction position of phase winding, x_{off} is turn-off position of phase winding, q is the number of phases, τ is the pole pitch of secondary side, and $x_{off} - x_{on} = \tau/2$.

The ampere turns formula is $N \cdot i = 2gB_g/\mu_0$, therefore the current can be expressed as

$$i = \frac{2 \cdot g \cdot B_g}{N \cdot \mu_0} \tag{3}$$

where g, B_g, and N are the air gap thickness, the average flux density in the air gap, and the number of turns in one winding, respectively.

The electrical dynamic of each phase can be written as

$$u = r \cdot i + \frac{\Delta\psi}{\Delta t} \tag{4}$$

where r represents the resistance of each winding, ψ denotes flux linkage of each winding, and time interval is calculated as $\Delta t = \tau/2v_m$. Because the resistance value is small, the voltage drop on the resistor can be ignored.

Under the linear model of the LSRM, the flux linkage variation from the aligned position to the unaligned position for a flat-topped (or square wave) phase current i is expressed by

$$\Delta\psi = (L_{as} - L_u) \cdot i \tag{5}$$

where L_{as} is the aligned saturated inductance per phase, L_u is the unaligned inductance per phase. Define the following variables: $\delta = L_{as}/L_a$, $\gamma = L_a/L_u$, where L_a is the aligned but unsaturated inductance.

Then the sector-winding voltage can be expressed as

$$u = \frac{\Delta\psi}{\Delta t} = L_{as} \cdot \left(1 - \frac{1}{\delta \cdot \gamma}\right) \cdot i \cdot \frac{2 \cdot v_m}{\tau} \tag{6}$$

The flux linkage at the aligned position is

$$\psi = L_{as} \cdot i = L_{pt} \cdot W_p \cdot B_g \cdot N \tag{7}$$

where W_p and L_{pt} are the primary stack thickness and the width of the primary intermediate teeth, respectively.

Therefore, the mechanical output power can be deduced as

$$P = 2 \cdot K_d \cdot \eta \cdot K_1 \cdot K_2 \cdot A_g \cdot v_m \cdot B_g \cdot A \tag{8}$$

where $K_1 = N_s/q$, N_s represents the number of secondary-side poles covered by the primary-side system and q is the number of phases, $K_2 = 1 - 1/\delta\gamma$, the pole area of the primary side is $A_g = L_{pt} \cdot W_p$, and A is the specific electric loading.

The primary size should meet the following rules: $W_s \geq W_p$, $\tau \geq W_s + W_p$, $q \cdot W_p \geq \tau$, therefore, W_p can be designed as $\tau/2 \geq W_p \geq \tau/q$. W_s is the secondary stack thickness, and it meets the followings condition: $\tau \cdot (q-1)/q \geq W_s \geq W_p$.

The pole pitch of the primary side is

$$W_{pp} = \frac{L_{pp} - W_p}{N_p - 1} \tag{9}$$

and the pole pitch of the secondary side is

$$\tau = \frac{N_p}{N_s} \cdot \frac{L_{pp} - W_p}{N_p - 1} \tag{10}$$

where L_{pp} is the primary length and Ns is the number of poles in the primary side.

The primary slot width is $L_{psw} = (W_{pp} - W_p)/2$, and the primary tooth width L_{ptw} is expressed as $L_{ptw} = L_{pt}/2$.

The slot depth of primary side with a slot filling-factor x nearer 30% should be

$$L_{psd} = \frac{N \cdot A_c}{x \cdot (W_{pp} - W_p)} \tag{11}$$

where A_c is the cross-section area of the coil wire.

For the designed linear motor, it is assumed that the pole distance on the primary side W_{pp} is 80 mm, the primary stack thickness W_p and secondary stack thickness W_s are equal to 40 mm, in addition, $q = N_p = 3$, and $N_s = 2$. It can be calculated the secondary pole pitch $\tau = 120$ mm and the primary slot width $L_{psw} = 20$ mm.

Affected by the installation process, the air gap of LSRM is generally larger than the rotary SRM, so the air gap thickness $g = 1$ mm is selected, and other constants are set as follows: $\eta = 0.65$, $K_1 = 2/3$, $K_2 = 0.75$, $K_d = 1.5$, $B_g = 1.4$ T, $A = 29400$ A/m. The pole area of primary side is obtained by

$$A_g = \frac{P}{2 \cdot K_d \cdot \eta \cdot K_1 \cdot K_2 \cdot v_m \cdot B_g \cdot A} \approx 1600\,\text{mm}^2 \tag{12}$$

The width of the primary intermediate teeth can be calculated as $L_{pt} = A_g/W_p = 40$ mm, then $L_{ptw} = 20$ mm.

The number of turns in the sector-winding is

$$N = \frac{\psi}{\phi_g} = \frac{u \cdot (x_{off} - x_{on})}{v_m \phi_g} = 225 \tag{13}$$

where $u = 20$ V, $\phi_g = B_g \cdot A_g = 2.24 \cdot 10^{-3}$ T $\cdot$ m^2, and $x_{off} - x_{on} = \tau/2 = 60$ mm.

The peak current is

$$i = \frac{2 \cdot g \cdot B_g}{N \cdot \mu_0} = 10\text{A} \tag{14}$$

J_m is the maximum allowable current density in the winding, the cross-section area of the coil wire is calculated as

$$A_c = \frac{i}{J_m \cdot \sqrt{q}} \approx 2\,\text{mm}^2 \tag{15}$$

According to equation (11), the slot depth of primary side $L_{psd} = 38$ mm. The initial dimensions of the motor are shown in Table 2.

TABLE 2. Calculation results of initial dimensions of motor.

Parameters	value (mm)
Primary tooth width (L_{ptw})	20
Primary slot depth (L_{psd})	38
Primary slot width (L_{psw})	20
Secondary tooth width (L_{stw})	20
Secondary slot depth (L_{ssd})	4
Secondary slot width (L_{ssw})	20
Primary stack thickness (W_p)	40
Secondary stack thickness (W_s)	40
Air gap (g)	1

IV. SENSITIVITY ANALYSIS AND OPTIMIZATION OF MOTOR SIZE PARAMETERS

After calculating the initial sizes of the LSRM, the primary and secondary size parameters of the LSRM are optimized by finite element calculations. The primary optimization parameters mainly include primary tooth width, primary slot depth, primary slot width and primary stack thickness. The secondary optimization parameters mainly include secondary tooth width, secondary slot depth, secondary slot width and secondary stack thickness. The optimizations are carried out in the order from primary to secondary, and from motor teeth to motor slots.

Before optimizing the above parameters, the optimization range shall be set according to the basic design principles of LSRMs. The electromagnetic thrusts of the motor under different sizes are calculated in turn. In this paper, the optimal size of each parameter is determined based on the average value of electromagnetic thrust of the motor. The optimization of motor parameters is completed on the premise that the total length and width of primary and secondary remain unchanged.

The optimizations of the size parameters of the designed motor are completed by static magnetic in Flux-3D software. Firstly, set the input constant current value of one-phase winding of the LSRM to 10 A. The travel interval of motor mover is set as half secondary cycle, i.e. 0 mm $\sim$ 60 mm. The calculation step of the finite element model of the motor is set to 2 mm. Then, the average electromagnetic thrust per unit mass of the motor under each size is calculated, and the calculation results are shown in Figure 7.

The optimized motor sizes are shown in Table 3. As shown in Figure 8, by comparing the electromagnetic thrusts of the LSRM before and after the optimizations, the maximum electromagnetic thrust per unit mass of the optimized motor is increased by 1.47 N/kg, and the average electromagnetic thrust per unit mass is increased by 0.38 N/kg.

V. LSRM PERFORMANCE COMPARISON OF DIFFERENT SECONDARY MATERIALS

In order to study the influence of different secondary materials on motor performance, according to the optimized motor sizes, the electromagnetic thrusts are calculated when the secondary materials are silicon steel sheet 50W470, No. 10 steel block, electrical pure iron DT2 and Q235 steel block respectively. The magnetization curves of four materials are shown in Figure 9.

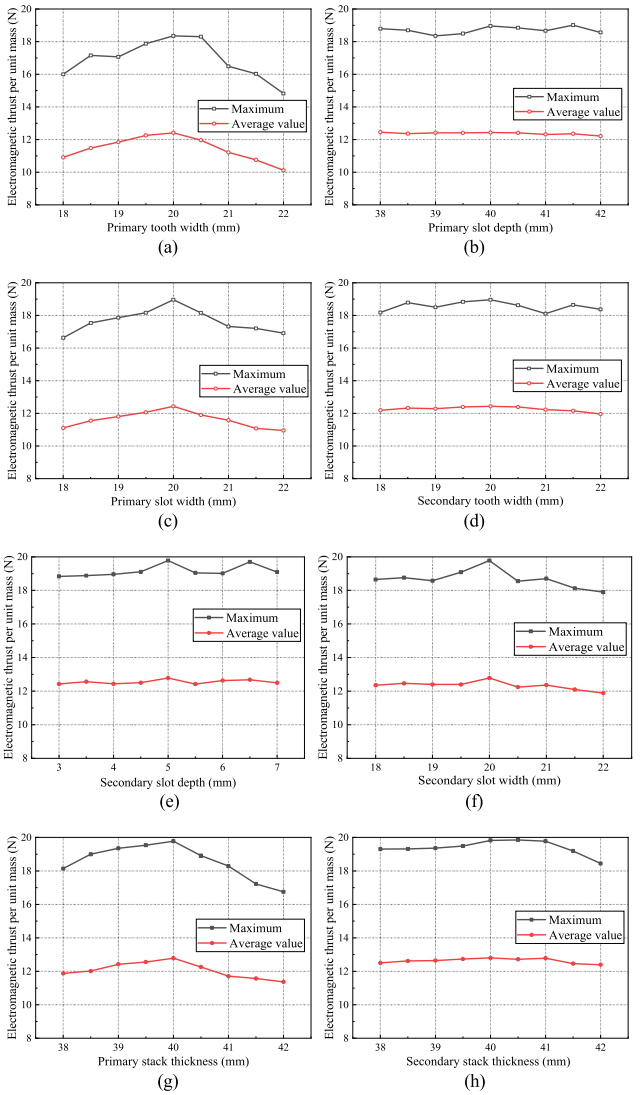

FIGURE 7. Average electromagnetic thrust per unit mass of the LSRM under different parameters of (a) Primary tooth width (L_{ptw}), (b) Primary slot depth (L_{psd}), (c) Primary slot width (L_{psw}), (d) Secondary tooth width (L_{stw}), (e) Secondary slot depth (L_{ssd}), (f) Secondary slot width (L_{ssw}), (g) Primary stack thickness (W_p), (h) Secondary stack thickness (W_s).

TABLE 3. Optimized initial dimensions of the LSRM.

Parameters	value (mm)
Primary tooth width (L_{ptw})	20
Primary slot depth (L_{psd})	40
Primary slot width (L_{psw})	20
Secondary tooth width (L_{stw})	20
Secondary slot depth (L_{ssd})	5
Secondary slot width (L_{ssw})	20
Primary stack thickness (W_p)	40
Secondary stack thickness (W_s)	40
Air gap (g)	1

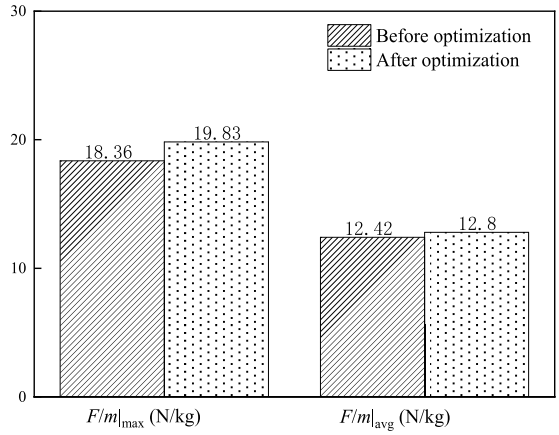

FIGURE 8. Comparison of electromagnetic thrust results before and after motor size optimization.

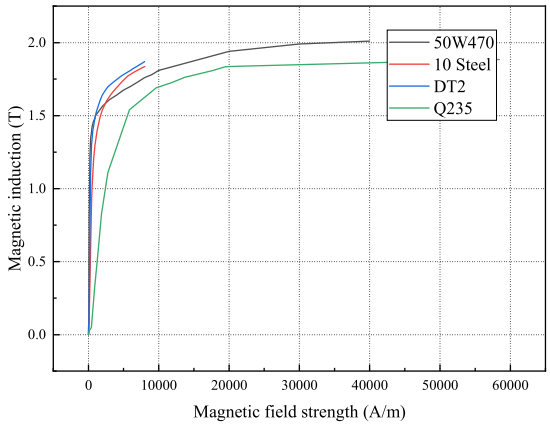

FIGURE 9. B-H curves of four secondary materials.

TABLE 4. Comparison of electromagnetic thrust of four LSRMs.

	50W470	DT2	No. 10 steel	Q235 steel
Thrust (5 A)	8.02 N	9.12 N	7.84 N	8.31 N
Thrust (10 A)	40.07 N	43.23 N	38.78 N	42.01 N
Thrust (15 A)	78.8 N	77.9 N	67.56 N	79.52 N

The electromagnetic field distributions of four secondary materials under different secondary positions and different current excitation are simulated and compared, and the electromagnetic thrust characteristic curves are obtained. When 5 A, 10 A and 15 A currents are respectively injected into the LSRM winding coil, the electromagnetic thrusts of the LSRMs with four secondary materials are shown in Figure 10. Table 4 lists the average electromagnetic thrust of the LSRMs with different materials under different excitation currents.

According to the Figure 10 and Table 4, when 5 A excitation current is applied to the motor, the motor core is in unsaturated state, and the electromagnetic thrust of the LSRM with electrical pure iron material is the largest, followed

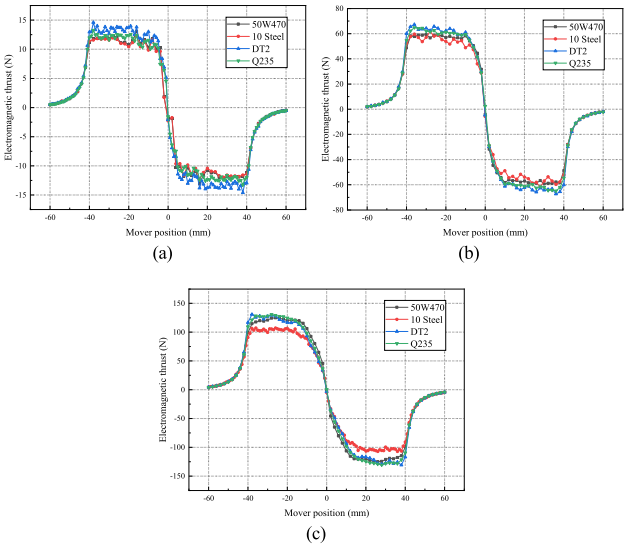

FIGURE 10. Calculation curves of electromagnetic thrusts under the excitation current of (a) 5 A, (b) 10 A, (c) 15 A.

by Q235 steel, silicon steel sheet and No. 10 steel. When the excitation current reaches 10 A and the motor works in the rated state, the electromagnetic thrust of the LSRM with electrical pure iron material is still the highest. The sequence of electromagnetic thrust of four LSRMs is the same as that of 5 A excitation current. When the excitation current reaches 15 A and the motor is in deep saturation state, the electromagnetic thrust of LSRM with the Q235 steel is the largest, followed by silicon steel sheet, electrical pure iron and No. 10 steel. The variation of electromagnetic thrust is mainly determined by the magnetization curve of the materials. In practical application, the selection of materials also needs to be comprehensively considered in combination with factors such as material price and corrosion resistance.

VI. MOTOR CONTROL

A. CONTROL WITH POSITION SENSORS

The operation of traditional LSRMs requires the position sensors to detect the relative positions of the mover in real time. In the position sensor control system of the designed LSRM in this paper, the eddy current sensor is selected to directly detect the relative positions of the mover, and each phase of motor is turned on and off according to the feedback signals of position sensors. Four eddy current sensors are used in the control system. The installation position of each sensor is 20 mm apart. The installation positions of the sensors are shown in Figure 11.

The three-phase inductance change curves of the LSRM prototype at different relative positions and the position square wave signals output by the position sensor are shown in Figure 12, where 0 mm position is the maximum inductance position of the phase C. According to the position sensor signals in one cycle (the secondary cycle is 120 mm), the selection method of LSRM conduction phases in this

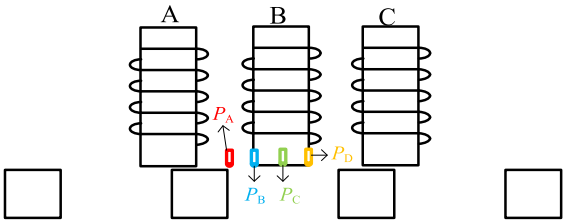

FIGURE 11. Installation diagram of position sensors.

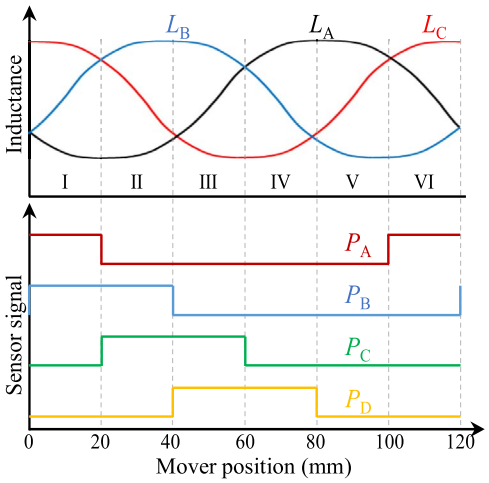

FIGURE 12. Position signals and phase inductance curves of the LSRM.

TABLE 5. Control logic of the LSRM with position sensors.

Regions	P_A	P_B	P_C	P_D	Excitation phase
I	1	1	0	0	B
II	0	1	1	0	A, B
III	0	0	1	1	A
IV	0	0	0	1	A, C
V	0	0	0	0	C
VI	1	0	0	0	B, C

scheme is given in Table 5. Taking area I as an example, when the mover moves to this area, the output signals of position sensors PA, PB, PC and PD are 1, 1, 0 and 0 respectively. At this time, phase B is in the inductance rising area, and phase A and C are in the inductance falling area. According to the basic control principle of LSRMs, the conducting phase is determined as phase B.

B. CONTROL WITHOUT POSITION SENSORS

The realization of the sensorless control of the LSRM will effectively improve the reliability of the system and reduce the maintenance cost of rail transit system. At present, LSRMs are still in the laboratory research stage, and the sensorless control strategies usually refer to the control methods of rotary SRMs. The LSRM designed in this paper is mainly used in the field of medium and low speed rail transit, so the

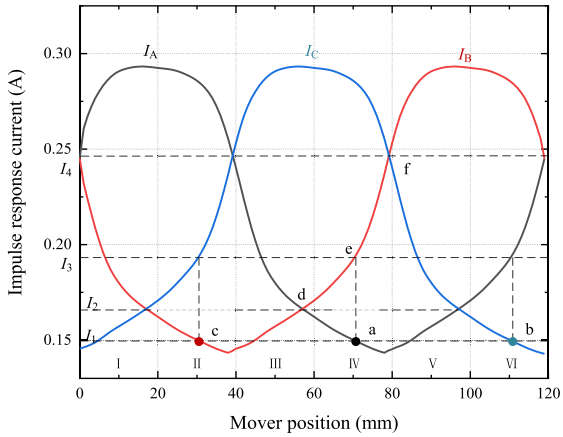

FIGURE 13. Three phase pulse response current curve.

TABLE 6. Control logic of the LSRM with no position sensor.

Regions	Order of I_A, I_B, I_C	Excited phases	Injected phases
I	$I_A>I_B\geq I_C$	B	C
II	$I_A\geq I_C>I_B$	$I_B\geq I_1$, B, A $I_B\leq I_1$, A	C
III	$I_C>I_A\geq I_B$	A	B
IV	$I_C\geq I_B>I_A$	$I_A>I_1$, A, C $I_A\leq I_1$, C	B
V	$I_B>I_C\geq I_A$	C	A
VI	$I_B\geq I_A>I_C$	$I_C>I_1$, C, B $I_C\leq I_1$, B	A

sensorless technology is realized based on the pulse injection method.

When pulse voltages are injected into the three phase windings of the LSRM prototype at the same time, the peak values of response currents are shown in Figure 13, where 0 mm position is the maximum inductance position of phase C. The peak values of the pulse response currents are directly proportional to the air gap reluctances of each phase magnetic circuit [26], [27], therefore, the change trend of response currents with relative positions are opposite to that of motor inductance curves. The minimum inductance position is the maximum pulse response current position, and the maximum inductance or fully aligned position is the position of minimum pulse response current. According to the relationship between three phase inductances or three phase pulse response currents in one cycle, the selection method of excitation and injection pulse phases of the LSRM are given in Table 6. The specific control methods are as follows:

1) Firstly, the high-frequency pulse voltages are injected into the three phase windings at the same time, and the pulse response currents I_A, I_B and I_C of the detection coils are obtained by using the current sampling circuit and the signal conditioning circuit;
2) According to the amplitude relationship between pulse response currents I_A, I_B and I_C, the secondary cycle of

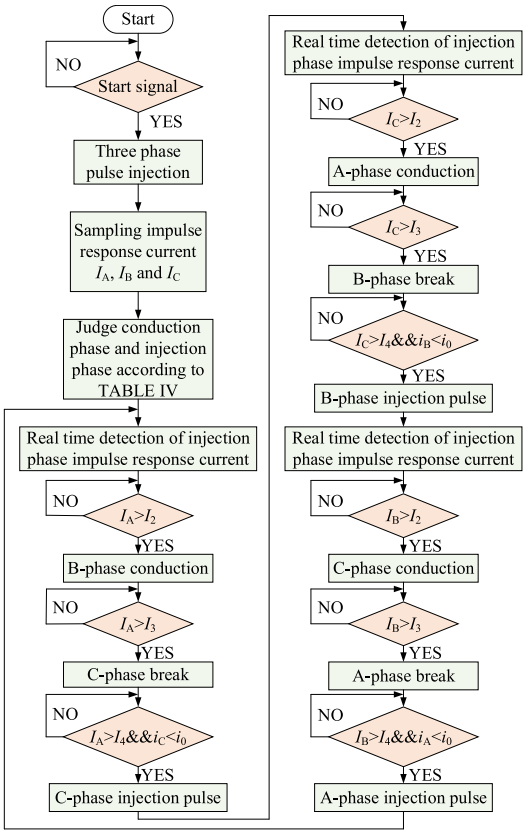

FIGURE 14. Flow chart of the sensorless control of the LSRM.

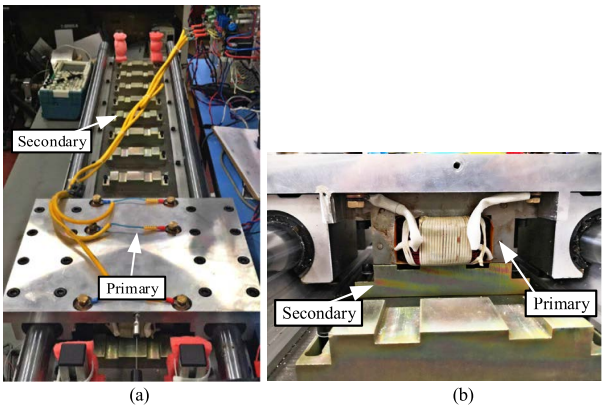

FIGURE 15. LSRM prototype photo (a) Overall picture (b) Primary and secondary main view.

the motor is divided into six regions, I ∼ VI. The selection methods of pulse injection phases and conduction phases corresponding to each region are described in Table 6;

3) In area II, in order to avoid excessive opening position during phase B startup, an opening position current threshold I_1 is set as shown in Figure 13. When I_B is greater than the threshold I_1, phase A and phase B are excited at the same time; When I_B is less than the threshold I_1, phase A is selected to be excited separately; Similarly, the starting methods in region IV and region VI are the same as that in region II. The intersections a, b and c of the threshold I_1 and the three-phase pulse response current curve are the turn-off position points of phase A, phase B and phase C in the three regions. By adjusting the threshold I_1, the turn-off positions of each phase during the LSRM startup can be adjusted.

The sensorless control methods after starting are as follows:

(1) When the motor is started, the non-reverse starting of the motor is realized according to the conduction phase given in Table 6, and the pulse response current values of the injection phase are detected in real time according to the injection phase given in the table;

(2) Taking the injection phase B as an example, when the pulse response current I_B of phase B is higher than the threshold I_2, as shown in point d in Figure 13, this position corresponds to the minimum inductance position of phase C of the motor. In this case, phase C is turned on;

(3) When the pulse response current I_B of phase B is higher than the threshold I_3, this position is the position of point e in Figure 13, that is, the maximum inductance position of phase A of the motor, phase A will be closed at this position;

(4) When the pulse response current I_B of phase B is higher than the threshold I_4, as shown in point f in Figure 13, this position corresponds to the minimum inductance position of phase A; In order to prevent the influence of the off phase residual current on the pulse injection signal, it is necessary to judge whether the residual current in phase A is lower than the threshold I_0 [18] after point f. when the residual current is less than the threshold I_0, the injection phase is changed to phase A;

(5) The motor control method based on injection phase A is to repeat steps (2) ∼ (4), and the specific judgment logic is described in flow chart 14. By changing the threshold I_2, the turn-on position of each phase can be changed, and by changing the threshold I_3, the turn-off position of each phase can be adjusted. I_2 and I_3 are at the position with high rising slope of pulse response current curve, so they have high position identification degree.

VII. EXPERIMENTAL RESULTS

The trial produced laboratory prototype is shown in Figure 15. The hardware platform of the control system is shown in Figure 16, which mainly includes controller, driving circuit, main circuit, isolation circuit, current detection circuit and auxiliary power module. In order to verify the accuracy of sensorless control, a linear encoder is installed on one side of the prototype. TI DSP TMS320F28335 is selected as the controller, and the optocoupler HCPL-3120 is used as the

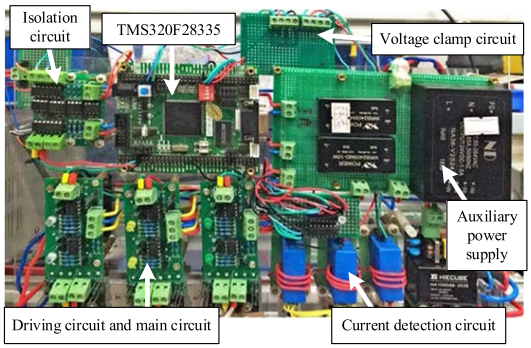

FIGURE 16. Hardware platform of control system.

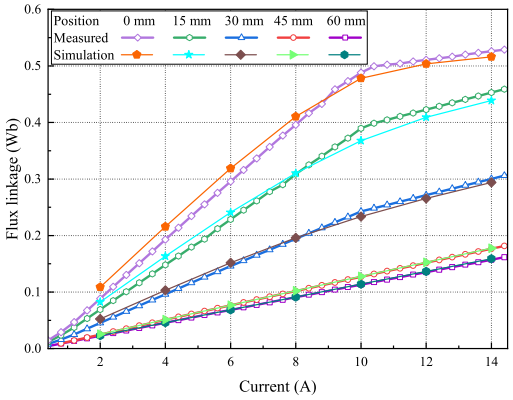

FIGURE 17. The measured curve and simulation calculation results of the flux linkages.

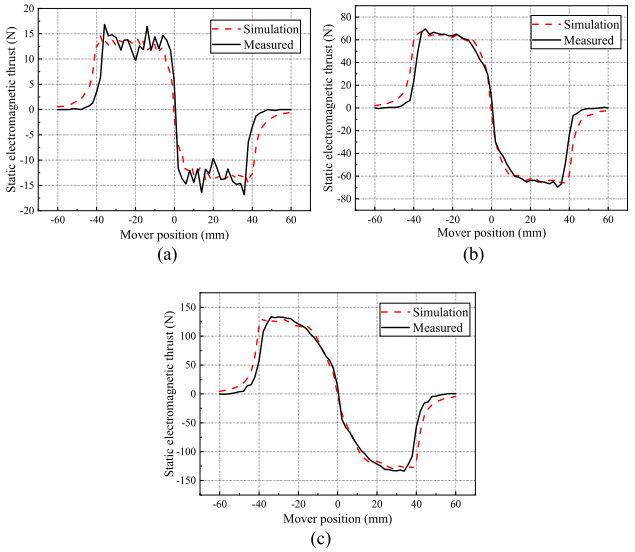

FIGURE 18. Measured and calculated electromagnetic thrusts under the excitation current of (a) 5 A, (b) 10 A, (c) 15 A.

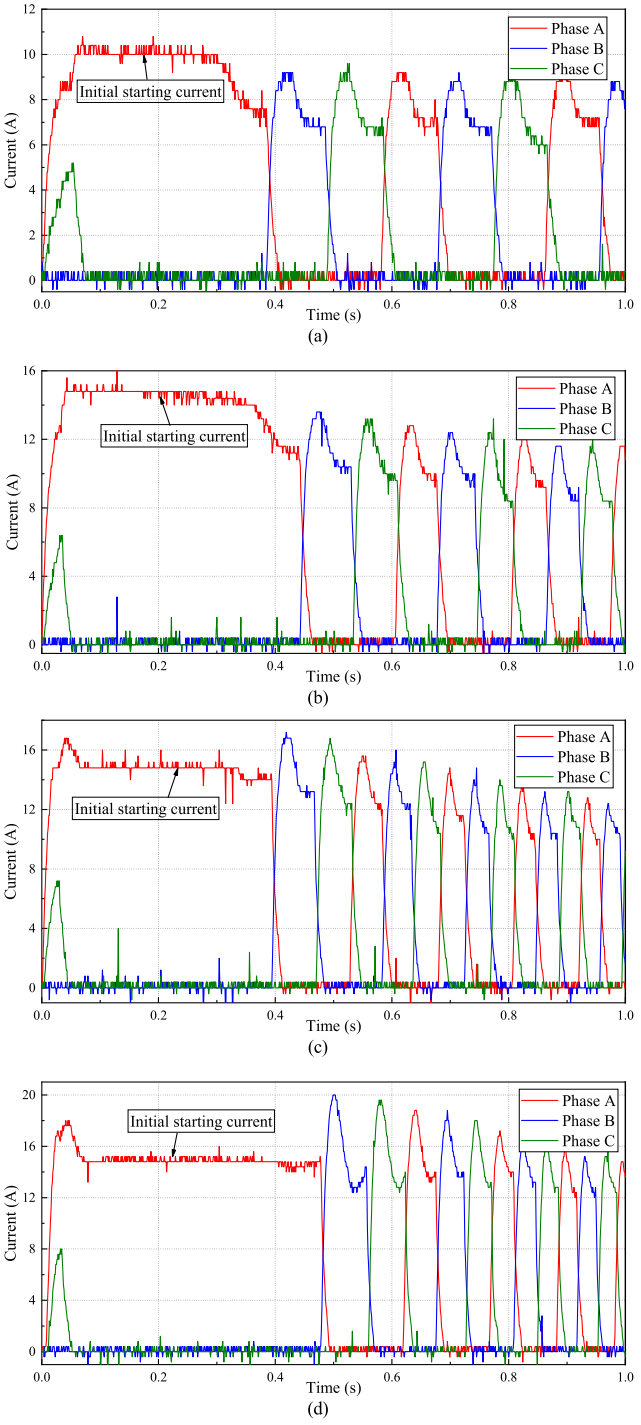

FIGURE 19. Three phase currents of the LSRM control system under excitation voltage of (a) 10 V, (b) 15 V, (c) 20 V, (d) 25 V.

driving chip in the driving circuit. The pulse response current and excitation current are detected by the current Hall sensor.

Firstly, the flux linkages of the motor from the minimum inductance position to the maximum inductance position are measured, in which 0 mm position is the maximum phase inductance position. The measured curve and simulation calculation results are shown in Figure 17. Secondly, the static electromagnetic thrusts of the motor are measured. The measured values and simulation calculated values are shown in Figure 18.

The measured static electromagnetic thrust and flux linkage of the motor basically coincide with the simulation

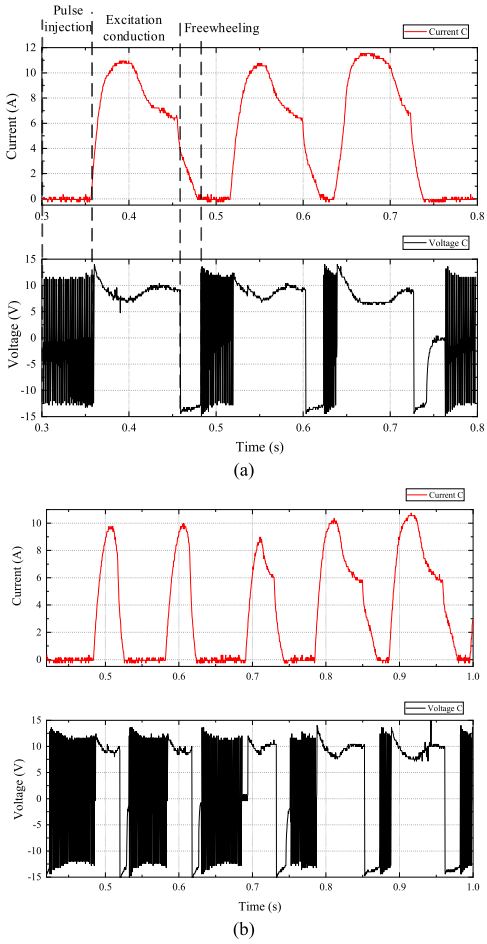

FIGURE 20. Phase voltage and current waveform of the LSRM sensorless control system under different average velocities (a) 0.833 m/s, (b) 1.18 m/s.

results, but there are errors in the non-coincidence area of the primary and secondary salient poles of the motor. The main reasons are as follows: (1) There will be some deviation between the motor material parameters set in the finite element software and the real parameters of the actual materials; (2) Prototype processing errors, such as air gap size, winding deviation and material processing error; (3) There will be measurement error and deviation caused by signal conditioning circuit in the measurement and reading process of pull pressure sensor and digital display instrument.

Figure 19 shows the current waveforms of three phase windings of the LSRM with position sensors under different excitation voltages. In this test, the motor operates in the open-loop state under no-load, the phase current increases with the excitation voltage, and the average value of phase current will become smaller with the increase of motor velocity. When the excitation voltage of the motor is 10 V, the peak current of each phase can reach 9 A; When the excitation voltage of the motor is 15 V, the peak current of each phase can reach 12 A; When the motor excitation voltage is rated voltage 20 V, the peak current of each phase can reach 16 A;

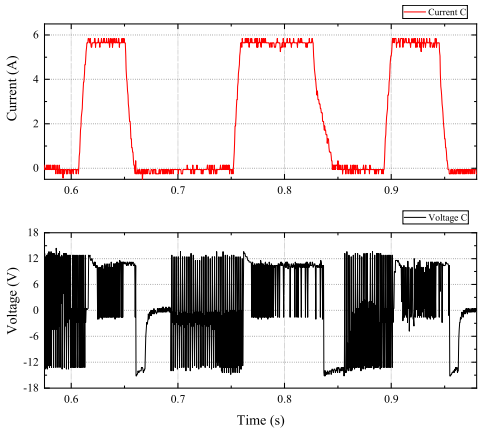

FIGURE 21. Phase voltage and current waveform during current chopping operation of the LSRM sensorless control system.

When the motor excitation voltage is 25 V, the peak current of each phase can reach 20 A. It can be seen that when the excitation voltage exceeds the rated voltage, the actual current value will exceed the set starting current limit. With the increase of motor running velocity, the motor phase current will gradually decrease.

Figure 20 show the voltage and current waveforms of phase C winding at different speeds when LSRM operates without position sensor. It can be seen from the waveform in Figure 20(a) that there are three stages of LSRM conduction phase: pulse voltage injection period, excitation conduction period and freewheeling period. Figure 20(b) shows the voltage and current variation curve of LSRM in the whole stroke (about 1 m). Due to the short motor stroke and the short motor acceleration process, the motor running state presents an acceleration-deceleration process. During deceleration, the phase winding current amplitude increases with the increase of phase winding excitation time.

In the process of motor starting, because the motor velocity is low and the starting current is large, the current chopper control needs to be added during the LSRM starting period to control the maximum amplitude of motor phase current. Figure 21 shows the phase voltage and current waveforms of the LSRM sensorless control system during current chopping operation. After the pulse injection is completed, the corresponding phase winding starts to be excited for current chopping control, and the current chopping threshold is set about 6 A in the test.

VIII. CONCLUSION

This paper attempts to study the application of LSRM in the field of long-distance rail transit. Firstly, the design and optimization method of the LSRM are introduced. Two structures of transverse flux LSRM are compared and analyzed by three-dimensional finite element software: EI type and EE type. The simulation results are analyzed and compared from the perspective of the average value of electromagnetic thrust per unit mass of the motor, and the structure of EE

type motor is optimized. The initial sizes of the motor are calculated by using the basic theory of SRM design. Through finite element analysis, the sensitivity of the optimized size parameters such as slot depth, slot width and tooth width of the motor is analyzed, and finally the size parameters of the motor are optimized. Then, the influence of different secondary materials on the basic characteristics of the motor is analyzed to provide guidance for the practical application of the motor. The LSRM laboratory prototype is trial manufactured, the hardware test platform is built, the flux linkage and electromagnetic thrust characteristics of the prototype are measured, and the electromagnetic thrust characteristics of motors with different secondary materials are compared. Finally, the sensorless control of LSRM is realized by pulse injection method. The experimental results verify the correctness of the motor design and control method.

REFERENCES

[1] G. Lv, T. Zhou, D. Zeng, and Z. Liu, "Design of ladder-slit secondaries and performance improvement of linear induction motors for urban rail transit," *IEEE Trans. Ind. Electron.*, vol. 65, no. 2, pp. 1187–1195, Feb. 2018.

[2] J.-M. Jo, S. Y. Lee, K. Lee, Y. J. Oh, S. Y. Choi, C.-Y. Lee, and K. Lee, "A position estimator using Kalman filter with a data rejection filter for a long-stator linear synchronous motor of maglev," *IEEE Access*, vol. 8, pp. 52443–52451, 2020.

[3] K.-H. Kim, H.-K. Cho, and D.-K. Woo, "3D characteristic analysis of 3-leg linear permanent magnet motor with magnet skew and overhang structure," *IEEE Access*, vol. 9, pp. 153863–153874, 2021.

[4] C.-T. Liu, K.-S. Su, and J.-W. Chen, "Operational stability enhancement analysis of a transverse flux linear switched-reluctance motor," *IEEE Trans. Magn.*, vol. 36, no. 5, pp. 3699–3702, Sep. 2000.

[5] G. Baoming, A. T. D. Almeida, and F. J. T. E. Ferreira, "Design of transverse flux linear switched reluctance motor," *IEEE Trans. Magn.*, vol. 45, no. 1, pp. 113–119, Jan. 2009.

[6] B.-S. Lee, H.-K. Bae, P. Vijayraghavan, and R. Krishnan, "Design of a linear switched reluctance machine," *IEEE Trans. Ind. Appl.*, vol. 36, no. 6, pp. 1571–1580, Nov. 2000.

[7] K. Diao, X. Sun, G. Lei, G. Bramerdorfer, Y. Guo, and J. Zhu, "Robust design optimization of switched reluctance motor drive systems based on system-level sequential Taguchi method," *IEEE Trans. Energy Convers.*, vol. 36, no. 4, pp. 3199–3207, Dec. 2021.

[8] J. Du, P. Lu, and D. Liang, "Optimal design of a linear transverse-flux machine with mutually coupled windings for force ripple reduction," *IET Electr. Power Appl.*, vol. 12, no. 2, pp. 271–780, Feb. 2017.

[9] G.-Z. Cao, N. Chen, S.-D. Huang, S.-S. Xiao, and J. He, "Nonlinear modeling of the flux linkage in 2-D plane for the planar switched reluctance motor," *IEEE Trans. Magn.*, vol. 54, no. 11, pp. 1–5, Nov. 2018.

[10] J.-H. Park, S.-M. Jang, J.-Y. Choi, S.-Y. Sung, and I.-J. Kim, "Dynamic and experimental performance of linear-switched reluctance machine with inductance variation according to airgap length," *IEEE Trans. Magn.*, vol. 46, no. 6, pp. 2334–2337, Jun. 2010.

[11] S. Darabi, Y. A. Beromi, and H. R. Izadfar, "Comparison of two common igurations of LSRM: Transverse flux and longitudinal flux," in *Proc. Int. Conf. Expo. Electr. Power Eng.*, Iasi, Romania, Oct. 2012, pp. 451–455.

[12] X. Sun, L. Feng, K. Diao, and Z. Yang, "An improved direct instantaneous torque control based on adaptive terminal sliding mode for a segmented-rotor SRM," *IEEE Trans. Ind. Electron.*, vol. 68, no. 11, pp. 10569–10579, Nov. 2021.

[13] L. Qiu, Y. Shi, B. Zhang, J. Pan, and X. Lai, "Tracking control of networked multiple linear switched reluctance machines control system based on position compensation approach," *IEEE Trans. Ind. Informat.*, vol. 14, no. 12, pp. 5368–5377, Dec. 2018.

[14] J. F. Pan, Y. Zou, N. Cheung, and G.-Z. Cao, "On the voltage ripple reduction control of the linear switched reluctance generator for wave energy utilization," *IEEE Trans. Power Electron.*, vol. 29, no. 10, pp. 5298–5307, Oct. 2014.

[15] J. Du, D. Liang, and X. Liu, "Performance analysis of a mutually coupled linear switched reluctance machine for direct-drive wave energy conversions," *IEEE Trans. Mag.*, vol. 53, no. 9, pp. 1–10, Sep. 2017.

[16] N. S. Lobo, H. S. Lim, and R. Krishnan, "Comparison of linear switched reluctance machines for vertical propulsion application: Analysis, design, and experimental correlation," *IEEE Trans. Ind. Appl.*, vol. 44, no. 4, pp. 1134–1142, Jul. 2008.

[17] H. S. Lim and R. Krishnan, "Ropeless elevator with linear switched reluctance motor drive actuation systems," *IEEE Trans. Ind. Electron.*, vol. 54, no. 4, pp. 2209–2218, Aug. 2007.

[18] S. Song, M. Zhang, L. Ge, and L. Wang, "Multiobjective optimal design of switched reluctance linear launcher," *IEEE Trans. Plasma Sci.*, vol. 43, no. 5, pp. 1339–1345, May 2015.

[19] D. Wang, X. Du, D. Zhang, and X. Wang, "Design, optimization, and prototyping of segmental-type linear switched-reluctance motor with a toroidally wound mover for vertical propulsion application," *IEEE Trans. Ind. Electron.*, vol. 65, no. 2, pp. 1865–1874, Feb. 2018.

[20] D. Wang, D. Zhang, X. Du, and X. Wang, "Unitized design methodology of linear switched reluctance motor with segmental secondary for long rail propulsion application," *IEEE Trans. Ind. Electron.*, vol. 65, no. 12, pp. 9884–9894, Dec. 2018.

[21] D. Wang, X. Wang, and X.-F. Du, "Design and comparison of a high force density dual-side linear switched reluctance motor for long rail propulsion application with low cost," *IEEE Trans. Magn.*, vol. 53, no. 6, pp. 1–4, Jun. 2017.

[22] Q. Wang, W. Jiang, X. Jing, and Z. Yu, "Sensorless control of segmented bilateral switched reluctance linear motor based on coupled voltage for long rail propulsion application," *IEEE Trans. Energy Convers.*, vol. 35, no. 3, pp. 1348–1359, Sep. 2020.

[23] Q. Wang, H. Chen, T. Xu, R. Nie, J. Wang, and S. Abbas, "Position estimation of linear switched reluctance machine with iron losses based on eddy-current effect," *IET Electr. Power Appl.*, vol. 10, no. 8, pp. 772–778, Sep. 2016.

[24] S. W. Zhao, N. C. Cheung, W. C. Gan, and J. M. Yang, "Position estimation and error analysis in linear switched reluctance motors," *IEEE Trans. Instrum. Meas.*, vol. 58, no. 8, pp. 2815–2823, Aug. 2009.

[25] X. Li and E. A. Mendrela, "Optimization of construction of linear switched reluctance motor with transverse magnetic flux," in *Proc. IEEE Region Conf.*, Kansas, MO, USA, Apr. 2008, pp. 1–5.

[26] G. Pasquesoone, R. Mikail, and I. Husain, "Position estimation at starting and lower speed in three-phase switched reluctance machines using pulse injection and two thresholds," *IEEE Trans. Ind. Appl.*, vol. 47, no. 4, pp. 1724–1731, Jul. 2011.

[27] A. Khalil, S. Underwood, I. Husain, H. Klode, B. Lequesne, S. Gopalakrishnan, and A. M. Omekanda, "Four-quadrant pulse injection and sliding-mode-observer-based sensorless operation of a switched reluctance machine over entire speed range including zero speed," *IEEE Trans. Ind. Appl.*, vol. 43, no. 3, pp. 714–723, May 2007.

XINLIANG LI received the B.S. degree from the School of Building Electrical and Intelligent Chemistry, Yangzhou University, Yangzhou, China, in 2020, where he is currently pursuing the M.S. degree in electrical engineering. His research interests includes integrated drive system control of switched reluctance linear motor.

FANG LIU received the B.S. degree from the School of Computer Science and Technology, China University of Mining and Technology, Xuzhou, China, in 2011. She is currently working as a Lecturer with the Yangzhou Polytechnic Institute, Yangzhou, China. Her current research interests include mechatronics and intelligent control algorithms.

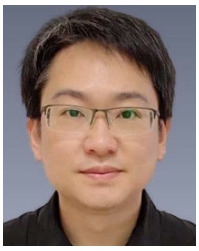

WEI JIANG (Member, IEEE) received the B.S. degree from Southwest Jiaotong University, Chengdu, China, in 2003, and the M.S. and Ph.D. degrees in electrical engineering from The University of Texas at Arlington, Arlington, TX, USA, in 2006 and 2009, respectively. From 2007 to 2008, he worked at EF Technologies LLC, as a Senior Design Engineer. In 2010, he joined Yangzhou University, as a Lecturer, and founded the Smart Energy Laboratory, where he is currently a Professor. He has been a Visiting Professor with Gunma University, Japan, in 2012; the University of Strathclyde; and Aston University, U.K., in 2015. He holds two U.S. patents and 13 Chinese patents. His current research interests include digitalized power conditioning to renewable energy and energy storage devices and microscopic analysis of electromechanical energy conversion.

HONG JIN received the Ph.D. degree in electrical engineering from Southeast University, Nanjing, China, in 2016. She is currently working as a Lecturer with Yangzhou University, Yangzhou, China. Her current research interests include design and control of ultrasonic motor and switched reluctance motor.

MINYAN LI received the B.S. degree in mechatronic engineering from the Nanjing University of Science and Technology, Nanjing, China, in 1996, and the M.S. degree in electrical engineering from Southeast University, Nanjing, in 1999. She is currently working as a Lecturer with Yangzhou University, Yangzhou, China. Her current research interests include computer control technology and motor control.

QIANLONG WANG received the B.S. and Ph.D. degrees from the School of Information and Electrical Engineering, China University of Mining and Technology, Xuzhou, China, in 2010 and 2016, respectively. He is currently working as a Lecturer with Yangzhou University, Yangzhou, China. His current research interests include design and control of rotary and linear switched reluctance machines.